Investigation of the O+allyl addition/elimination reaction pathways from the OCH$_2$CHCH$_2$ radical intermediate

Benjamin L. FitzPatrick,[1] Kai-Chung Lau,[1,a)] Laurie J. Butler,[1,b)] Shih-Huang Lee,[2] and Jim Jr-Min Lin[3]

[1]*The James Franck Institute and Department of Chemistry, University of Chicago, Chicago, Illinois 60637, USA*
[2]*National Synchrotron Radiation Research Center, Hsinchu, 30076 Taiwan, Republic of China*
[3]*Institute of Atomic and Molecular Sciences, Academia Sinica, Taipei, 10617 Taiwan, Republic of China*

These experiments study the preparation of and product channels resulting from OCH$_2$CHCH$_2$, a key radical intermediate in the O+allyl bimolecular reaction. The data include velocity map imaging and molecular beam scattering results to probe the photolytic generation of the radical intermediate and the subsequent pathways by which the radicals access the energetically allowed product channels of the bimolecular reaction. The photodissociation of epichlorohydrin at 193.3 nm produces chlorine atoms and c-OCH$_2$CHCH$_2$ radicals; these undergo a facile ring opening to the OCH$_2$CHCH$_2$ radical intermediate. State-selective resonance-enhanced multiphoton ionization (REMPI) detection resolves the velocity distributions of ground and spin-orbit excited state chlorine independently, allowing for a more accurate determination of the internal energy distribution of the nascent radicals. We obtain good agreement detecting the velocity distributions of the Cl atoms with REMPI, vacuum ultraviolet (VUV) photoionization at 13.8 eV, and electron bombardment ionization; all show a bimodal distribution of recoil kinetic energies. The dominant high recoil kinetic energy feature peaks near 33 kcal/mol. To elucidate the product channels resulting from the OCH$_2$CHCH$_2$ radical intermediate, the crossed laser-molecular beam experiment uses VUV photoionization and detects the velocity distribution of the possible products. The data identify the three dominant product channels as C$_3$H$_4$O (acrolein)+H, C$_2$H$_4$+HCO (formyl radical), and H$_2$CO (formaldehyde)+C$_2$H$_3$. A small signal from C$_2$H$_2$O (ketene) product is also detected. The measured velocity distributions and relative signal intensities at m/e=27, 28, and 29 at two photoionization energies show that the most exothermic product channel, C$_2$H$_5$+CO, does not contribute significantly to the product branching. The higher internal energy onset of the acrolein+H product channel is consistent with the relative barriers en route to each of these product channels calculated at the CCSD(T)/aug-cc-pVQZ level of theory, although a clean determination of the barrier energy to H+acrolein is precluded by the substantial partitioning into rotational energy during the photolytic production of the nascent radicals. We compare the measured branching fraction to the H+acrolein product channel with a statistical prediction based on the calculated transition states. © 2008 American Institute of Physics. [DOI: 10.1063/1.2966004]

I. INTRODUCTION

There is a wealth of experiments probing the detailed reaction dynamics of small molecules. However elucidating the dynamics of radical-radical reactions, which can occur via competing direct abstraction and addition/elimination pathways, is difficult. Such reactions play a fundamental role in combustion chemistry, especially low temperature combustion where the nearly barrierless addition/elimination pathways characteristic of radical-radical reactions can dominate the product branching. The reaction of ground state oxygen atoms with CH$_2$CHCH$_2$ (allyl radicals) is particularly interesting because it contrasts the barrierless entrance channel of a radical-radical reaction with the relative stability of

the resonance stabilized[1] allyl radicals. (In contrast, the rate of reaction of allyl radicals with molecular oxygen is small.[2–4]) Additionally, allyl radicals are thought to be major contributors to the initial steps in soot formation, the generation of small aromatic molecules.[1,5–7]

Previous works on the O(^3P)+C$_3$H$_5$ reaction studied the bulk kinetics,[8] the products formed in crossed molecular beam experiments,[9–14] and the ground state potential energy surface via electronic structure calculations.[15] The experiments thus far have not been able to identify all the important product channels in this bimolecular reaction, although most studies conclude that H+acrolein is an important contributor to the product branching. The prior work began with that of Slagle *et al.*,[8] who used laser flash photolysis in mixtures of photolytic precursors to O atoms and allyl radicals to measure the reaction rate as a function of temperature and pressure. They attempted to determine what product channels were important using photoionization mass spectrometry.

---

a)Present address: Department of Biology and Chemistry, City University of Hong Kong.
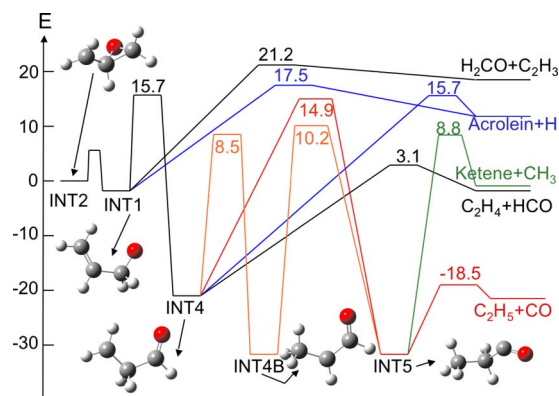b)Electronic mail: L-Butler@uchicago.edu

FIG. 1. (Color online) Partial potential energy surface for O+allyl calculated at the RCCSD(T)/aug-cc-pVQZ‖UCCSD/aug-cc-pVDZ level of theory. All energies are in kcal/mol, corrected for the zero point energy, and relative to INT2, which is set as the zero of energy.

They used several lamp sources to allow them to detect all the possible product channels, five of which are shown in Fig. 1, but concluded that only the acrolein signal had a time profile consistent with being a primary product. Even without the advantage of having a prediction based on electronic structure theory, they correctly anticipated that the H_2CO +C_2H_3 channel might be an important one, but they did not see any signal from either H_2CO or C_2H_3; hence they concluded that this channel was less than 20% of the yield of the acrolein+H product channel. They correctly concluded that the lack of a pressure dependence in their measured rate constants indicates that when a radical intermediate is formed, it irreversibly goes on to products (it is not stabilized by collisions). The reaction O+allyl→acrolein+H is exoergic by 64 kcal/mol; so all of the intermediate barriers shown in Fig. 1 are well below the reactant asymptote. The next most significant work on this system was that of Choi and co-workers.[9–12] That study used a crossed molecular beam apparatus to detect only the primary products (as opposed to the secondary product formed in bulk mixtures), but they only attempted to detect OH products[9,10] [that apparatus used laser-induced fluorescence (LIF) detection only, not electron bombardment or single photon ionization detection]. Interestingly, they did detect OH product, although the OH +allene product asymptote is 20 kcal/mol higher in energy than the acrolein+H product channel, and they conclude from the bimodal rotational energy distributions of the OH product that this minor product channel occurs via a competition between a direct abstraction channel and an indirect short-lived addition complex forming reaction. To support their interpretation they calculated the relevant minima and transition states on the global potential energy surface for the reaction at the CBS-QB3 level of theory.[13] Their Rice–Ramsperger–Kassel–Marcus (RRKM) rates from the OCH_2CHCH_2 radical intermediate suggest that the branching to the H_2CO+C_2H_3 product channel should be nearly equal to that of acrolein+H (7.4/8.4 for the collision energy used in the molecular beam experiment), in contrast to the experimental results of Slagle *et al.*[8] Later work[11] in the same group detected H-atom products using vacuum ultraviolet (VUV)-LIF at 121 nm, attributing them to the H +acrolein product channel.

In 2006–2007, Casavecchia and co-workers[14,15] studied the product channels in the O+allyl reaction in a crossed molecular beam scattering apparatus with low-energy electron bombardment ionization of the products. Although this versatile experimental technique provided compelling results for the qualitatively similar reaction of O+ethene, product identification in the O+allyl studies was problematic. Their 2007 paper concluded that acrolein+H is a definitive product channel, but they were unable to definitely assign the signal detected at $m/e=27$ and 29. They conclude that "one or more C–C bond breaking channels" contribute to the product branching.

Our work presented here seeks to determine the product channels resulting from a specific radical intermediate of the O+allyl reaction, which forms upon addition of the O atom to one of the end carbons rather than the central carbon. We first characterize the photolytic production of the radical, photodissociating C_3H_5ClO (epichlorohydrin) at 193.3 nm to yield a Cl atom and the cyclic radical labeled INT2 in Fig. 1; the vibrationally excited cyclic radical easily isomerizes under collision-free conditions to form the O atom adduct OCH_2CHCH_2 labeled INT1 in Fig. 1 (the ring opening could also occur concertedly with the C–Cl fission). The experiments characterize the velocity and internal energy distributions of these radicals, and then probe the resulting products from the internally excited radical intermediate. As the dynamics relevant to the bimolecular reaction is initiated in this radical adduct, our experiments do not probe the direct abstraction channels in the O+allyl reaction, but rather the addition/elimination pathways important upon addition to the terminal C atom. Thus, the data provide definitive measurements that are complementary studies of the full bimolecular collision. As is apparent within, they further allow one to elucidate the addition/elimination pathways on the global potential energy surface from specific radical addition complexes to the final product channels accessed by the O atom addition to the terminal C atom in this experiment. Thus, they shed light on the origin of the product branching observed in crossed beam or kinetics measurements.

II. EXPERIMENT

All three of the experimental apparatuses have been detailed in previous publications cited below, so only the salient features shall be discussed below. The crossed laser-molecular beam instruments are quite similar; hence the details from the electron impact apparatus, if different, will be given inside of square brackets after the corresponding part or parameter is listed for the VUV ionization apparatus. Unfamiliar readers may refer to an overview of photodissociation dynamics given in a review by Butler and Neumark[16] in order to gain a better understanding of the experimental setups and the data they measure.

The velocity distributions of the Cl atoms and C_3H_4O ($m/e=56$) radical photofragments of epichlorohydrin were measured with the rotating-source, crossed laser-molecular beam apparatus[17–21] on the 21A1 U9/Chemical Dynamics beamline at the National Synchrotron Radiation Research Center (NSRRC) located in Hsinchu, Taiwan (the electronic

impact apparatus[21] is located at the University of Chicago). A Lambda Physik LPX 220 ArF laser (Lumonics PM-848 ArF laser), operating at 193.3 nm, produced momentum-matched Cl atoms and C_3H_5O radicals by photodissociation of epichlorohydrin, Fluke$>$98% purity (Acros$>$98%). The laser operated at 70 Hz (100 Hz) with a measured per pulse energy for each spectrum ranging from 10 to 12 mJ (20–30 mJ). This is below the saturation level of epichloro-hydrin, which has a small absorption cross section of about 10^{-19} cm^2. The focused laser beam was a rectangle 8.5 mm tall by 2.5 mm wide (3×2 mm^2), which intersected the $\sim$3 mm diameter molecular beam. The molecular beam, consisting of room temperature epichlorohydrin seeded in helium having a backing pressure of 800 torr (650 torr), was expanded through an Even-Lavie (Parker General) pulsed valve. The pulsed valve had an orifice 0.4 mm (0.5 mm) in diameter, which was heated to 110 °C (90 °C).

The molecular beam's speed distribution at the point where photodissociation occurred was determined using a chopper wheel nominally operating at 200 Hz (300 Hz). The short flight path in the apparatus at the NSRRC necessitated taking considerable care in measuring the timing offsets inherent in the measurement (e.g., the molecular beam passed a chopper slit a quarter revolution after the photodiode sync pulse, so correcting for a rotational frequency of 199 rather than 200 Hz results in a 6.28 μs difference). The peak in the number density distribution of molecular speeds was 1620 m/s with a full width at half maximum (FWHM) of 28.3% (1420 m/s with a FWHM of 14.1%). Only a small number of recoiling photofragments, those having the proper velocity after photodissociation to enter the detector, crossed the 10.05 cm (44.6 cm) neutral flight path where tunable VUV synchrotron radiation (200 eV electrons) ionized them. Photoionization energies were tuned with the U9 undulator gap, and a 7 mm diameter circular aperture defined the VUV beam. In this work a 33 mm gap was used to obtain a nominal photoionization energy of 13.79 eV, but it should be noted that the actual maximum of intensity was at 13.77 eV. (Refer to our previous publication regarding ethyl chloride[22] for a more complete discussion of this recalibration.) Likewise, the undulator gap of 31.25 mm for a nominal energy of 12.14 eV was recalibrated to 12.08 eV. A rare gas filter (Ar and Kr) operated at approximately 10 torr filtered out higher harmonics of the VUV. After traveling through the ionizing region, the photofragments were mass selected using an Ex-trel 1.7 MHz (Extrel model 13 High-Q head) quadrupole mass spectrometer and were counted by a Daly detector.[23] A multichannel scaler recorded the total time of flight (TOF) of the photofragments spent in traveling from the interaction region to the Daly detector. There was a time lag of 1.54 μs between triggering of the multichannel scaler and firing of the laser for which all TOF spectra and associated fits are corrected. The flight times depicted in the figures herein are the sum of the neutral photofragment flight time (from a velocity determined by the vector sum of the center-of-mass velocity, the recoil velocity imparted to the Cl and OCH_2CHCH_2 photofragments and, for bimolecular products, the recoil velocity imparted to the product as the radical dissociates) and the ion flight time through the mass spec-

trometer. The latter is calculated using the apparatus' measured ion flight constant of 5.40 μs amu$^{-1/2}$ (4.5 μs amu$^{-1/2}$). The recoil translational energy distribution from the C–Cl bond fission is determined by creating a forward convolution fit to the TOF spectra. Finally, the conservation of energy yields an internal energy distribution of the nascent C_3H_5O radicals.

To resolve the spin-orbit state of the Cl atoms and their individual velocity distributions, we used the two-dimensional photofragment velocity map ion imaging apparatus with resonance-enhanced multiphoton ionization (REMPI) photoionization detection of the Cl atoms. The experimental method[24–26] has been described in detail previously and used in several studies[27–29] in our laboratory. Samples of epichlorohydrin were purchased from Aldrich and used without further purification. The sample was introduced into the photodissociation region in the form of a seeded and skimmed supersonic beam. The helium was bubbled through the epichlorohydrin, forming a 10% seeded beam, prior to the expansion through a pulsed valve (nozzle diameter $\approx$0.6 mm) at a stagnation pressure of 500 torr.

The 532 nm output of a Nd:YAG (yttrium aluminum garnet) laser (Continuum PL9020) was used to pump a dye laser (Lambda Physik, FL3002, LDS698 dye), which generated visible radiation in the region of 675–715 nm. The dye laser output was frequency doubled in a potassium dihydrogen phosphate crystal, and the resulting 353 nm light was mixed with the 706 nm fundamental in a beta-barium borate crystal, producing the 235 nm UV radiation. A focusing lens (focal length $\approx$109 mm) was used to focus the 235 nm laser into the chamber. The 235 nm light was linearly polarized along an axis vertically perpendicular to the molecular beam and parallel to the detector surface. A 193.3 nm ArF excimer laser (GAM EX10F/300), counterpropagated with the REMPI light, was focused into the reaction chamber by a focusing lens (focal length $\approx$50 mm); this light was used to photodissociate the epichlorohydrin sample. The atomic Cl($^2P_{1/2}$) and Cl($^2P_{3/2}$) fragments were then ionized via [2+1] REMPI at 235.20 nm ($4p\ ^2P_{1/2} \leftarrow 3p\ ^2P_{1/2}$) and 235.34 nm ($4p\ ^2D_{3/2} \leftarrow 3p\ ^2P_{3/2}$), respectively. During the experiment, the pulse energy ($\approx$0.5 mJ) of the 235 nm laser beam was reduced substantially to minimize Coulomb repulsion between the ions formed in the photodissociation region.

The spherically expanding ion cloud formed during photodissociation was accelerated toward a two-dimensional position-sensitive detector by an electrical ion lens assembly having a repeller/extractor voltage ratio of 1.404. After traveling through the TOF drift region ($\approx$577 mm), the ions were collected by a detector (Burle 3040FM) consisting of two chevron microchannel plates (MCPs) coupled to a P20 phosphor screen via fiber optics. In order to detect only the ions of interest, the front MCP voltage was gated by applying a negative voltage pulse at the appropriate time. The pulse is -750 V in magnitude and 70 ns in width. The phosphor screen was maintained at 3.5 kV above the potential of the rear MCP. Images appearing on the phosphor screen were recorded by a 1376×1040 pixel charge-coupled device cam-

era (LaVision Imager 3) with a standard 35 mm camera lens. The ion signal was obtained using the event-counting algorithm in the DAVIS software, and each image was accumulated for over 100 000 laser shots. The timing sequence for opening of the pulsed valve, firing the Nd:YAG and excimer lasers, pulsing the MCP, and capturing the ion images was controlled by a digital pulse generator (Stanford Research DG535) at a repetition rate of 20 Hz. During the detection of the $Cl(^2P_{1/2})$ and $Cl(^2P_{3/2})$ fragments, the laser was scanned over the Doppler profile. Reconstruction of the images into three-dimensional scattering distributions was performed using the Gaussian basis-set expansion Abel transformation method developed by Dribinski *et al.*[30]

III. RESULTS AND ANALYSIS

A. Photolytic generation of the radical intermediate

This experiment begins with investigating the photolytic generation of the OCH_2CHCH_2 radical intermediate from the following photodissociation reaction:

$$c\text{-}OCH_2CHCH_2Cl \rightarrow c\text{-}OCH_2CHCH_2 + Cl(^2P_{3/2,1/2}).$$

$$(1)$$

The primary product is a radical in which the O atom bridges the center and one end C atom (INT2 in Fig. 1). The photodissociation produces a rotationally and vibrationally excited radical whose internal energy distribution is characterized by measuring the velocity of the momentum-matched Cl atom; the radical then undergoes a facile ring opening to form the straight chain OCH_2CHCH_2 radical labeled INT1 in Fig. 1. (This ring opening may also occur during C–Cl bond fission.) The bond dissociation energy (D_0) for the C–Cl bond fission channel is calculated at the Gaussian-3 (G3‖B3LYP) (Refs. 31 and 32) level of theory using the GAUSSIAN03 package.[33]

The geometries and the associated frequencies in Fig. 1 were calculated with the UCCSD/aug-cc-pVDZ level of theory using GAUSSIAN03 because it has analytic gradients. All geometry optimizations were performed without symmetry starting from both the *cis* and *trans* isomers so as to reduce the likelihood of only finding local minima. The geometries were converged to a root-mean-square (rms) force below 1×10^{-6} and a rms displacement below 4×10^{-6}, where both are in a.u. Intrinsic reaction coordinate calculations were performed at the B3LYP/aug-cc-pVTZ level of theory for each transition state to make sure it corresponds to the correct reactants and products. Restricted, open-shell coupled cluster single point energies, RCCSD(T), were calculated using the MOLPRO package[34,35] with ROHF and correlation energies converged to less than 1 μ hartree. The single point energies include the zero point energy correction based on the unscaled UCCSD/aug-cc-pVDZ frequencies. All of the relevant structures (including conformers not shown in Fig. 1), moments of inertia, and vibrational frequencies are given in the supplementary EPAPS document.[36]

The internal energy distribution of the nascent C_3H_5O radicals is calculated from the measured product recoil translation energy, E_T, using

$$E_{int}(c\text{-}OCH_2CHCH_2) = E_{int}(c\text{-}OCH_2CHCH_2Cl)$$
$$+ h\nu - D_0(c\text{-}OCH_2CHCH_2 - Cl)$$
$$- E_T - E_{so}.$$

$$(2)$$

The vibrational energy content of epichlorohydrin [i.e., $E_{int}(c\text{-}OCH_2CHCH_2Cl)$] at 298 K is estimated to be 1.4 kcal/mol (2.5 kcal/mol at 383 K) using the harmonic vibrational frequencies calculated at the B3LYP/6-31G(d) level and scaled by a factor of 0.96. We assume that the supersonic expansion effectively cools down the rotational motions but not the vibrations. There are three possible conformers of the precursor molecule with different orientations of the chloromethyl group with respect to the cyclic ring. G3‖B3LYP calculations predict that the relative stability of these three conformers differ by 0.6–1.2 kcal/mol. Thus, the conformers are indistinguishable, given the experimental uncertainty in this study and the accuracy of the theoretical methods employed here. The photon energy, $h\nu$, is 147.8 kcal/mol for 193.3 nm light. $D_0(c\text{-}OCH_2CHCH_2-Cl)$ is calculated at the G3‖B3LYP level to be 80.1 kcal/mol [the energy difference between the most stable conformer of epichlorohydrin and the radical+$Cl(^2P_{3/2})$]. (We also calculated the C–Cl bond energy using the CCSD geometries and complete basis set extrapolations for the energies; this gives a value only 1 kcal/mol higher.) E_{so} can be 0 or 2.5 kcal/mol, corresponding to the ground spin-orbit state ($^2P_{3/2}$) and excited state ($^2P_{1/2}$) of the Cl atom. The relative populations of each are determined as a function of E_T by the data in Sec. III F.

B. Determining the internal energy distribution of the nascent radicals

To determine the internal energy of the radicals probed in our experiments, we use energy conservation as shown in Eq. (2). We need only measure the distribution of recoil kinetic energies E_T, imparted between the Cl atom and the momentum-matched radical by detecting the Cl atom velocity distribution. The figures herein show data taken using the molecular beam scattering apparatus with VUV ionization unless otherwise noted. Figure 2 shows the forward convolution fit to the Cl$^+$ TOF spectrum at $m/e=35$. The distribution is bimodal with a sharp, fast peak at approximately 60 μs corresponding to the solid line and a small slow, broad feature peaking near 90 μs, the dashed line. The two distinct distributions are also apparent in Fig. 3, which displays the recoil kinetic energy (KE) distribution resulting from the forward convolution fit to the data in Fig. 2. The high KE component, in solid line, has a maximum at about 33 kcal/mol and comprises 87% of the total. The low KE portion of the distribution (for C–Cl fission events forming higher internal energy radicals), in dashed line, has a maximum near 1 kcal/mol and comprises 13% of the total. The separation of the $P(E_T)$ into two parts is approximate in regions where they overlap; we show below that the minor low recoil KE portion of the distribution produced radicals that do not dissociate to H+acrolein, so we used fits of the acrolein data to determine the high KE component in the overlapping regions. Using Eq. (2) and the imaging results described in the
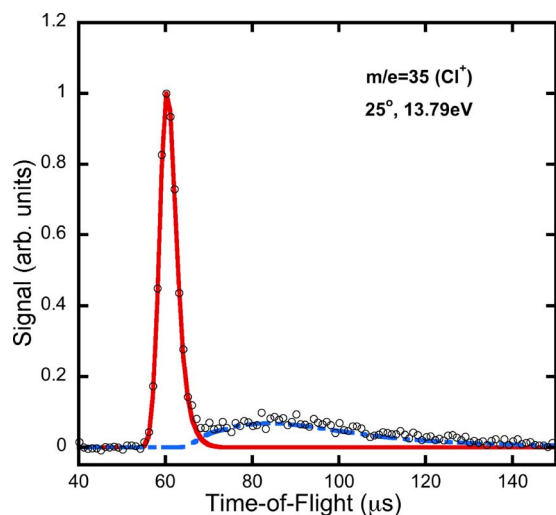
FIG. 2. (Color online) TOF spectrum of $m/e=35$ at a source angle of 25°. The data, with constant background subtracted, were accumulated for 275 000 laser shots. The open circles correspond to the data points and the solid and dot-dashed lines represent the forward convolution fits to the spectrum from the $P(E_T)$ given in Fig. 3.

FIG. 4. (Color online) Chlorine spectrum taken at the University of Chicago using electron bombardment ionization and 1×10^6 shots with constant background subtraction. The open circles are the data points, and the solid line is the fit calculated from the solid line portion of the $P(E_T)$ in Fig. 3. The low recoil KE portion of the $P(E_T)$ is not used because the pulsed nozzle created a nonconstant background at longer flight times, so the data are not high enough quality to discern that contribution.

next section to determine the spin-orbit state of the Cl atom at each recoil KE, this $P(E_T)$ for the C–Cl bond fission is converted to a distribution of internal energies in the nascent radicals ranging from 17 to 70 kcal/mol with a maximum at 38 kcal/mol. The chlorine spectrum taken using VUV ionization is compared with one using electron impact ionization because the latter ionizes all species democratically, independent of quantum state(s) of the photofragment. Figure 4 presents the electron impact ionization TOF spectrum of chlorine where the source region is rotated 15° above the detector axis. The quality of the fit to the fast peak is quite good, indicating that no preferential ionization takes place when using broad-linewidth tunable VUV near 13.8 eV for detecting $Cl(^2P_{3/2})$ and $Cl(^2P_{1/2})$. Unfortunately, a similar
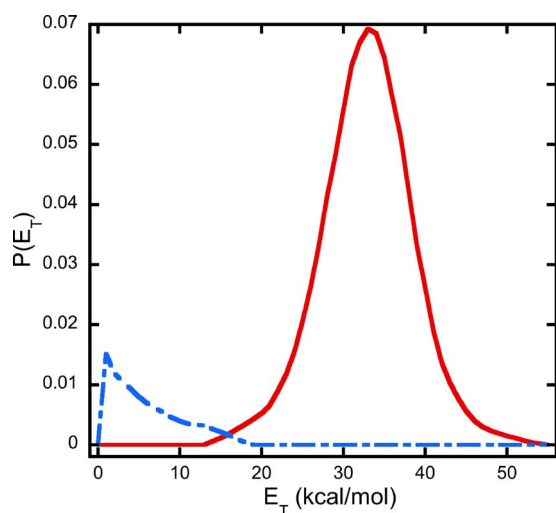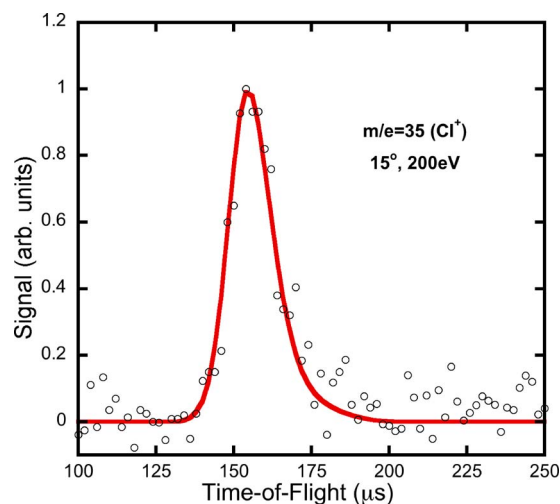

FIG. 3. (Color online) Total recoil KE distribution derived from forward convolution fitting the $m/e=35$ data shown in Fig. 2. The high recoil KE portion of the distribution shown in solid line corresponds to C–Cl fission events that produce radicals that subsequently access the H+acrolein product channel. In contrast, the lower recoil KE portion of the distribution shown in dot-dashed line does not.

characterization of the slower peak could not be made because an uneven background grew in at longer flight times and could not be subtracted out due to lack of insufficient data collected with the laser off.

C. The H+acrolein product channel from the selected radical intermediate

As expected from the fact that we produce all the nascent radicals with enough internal energy to isomerize to straight chain OCH_2CHCH_2 and dissociate to one or more product channels of the O+allyl bimolecular reaction (see Fig. 1), we do not detect signal (integrating for $>225 000$ shots) at the stable C_3H_5O radical mass ($m/e=57$). However, since the acrolein+H product channel involves only loss of a H atom, we expect the acrolein ($m/e=56$) velocity to be nearly identical to the velocity of the radical that dissociated to give that product. Thus we can use the $P(E_T)$ in Fig. 3 to predict the velocities of the momentum-matched radicals to the Cl atoms formed in the primary photodissociation producing the high internal energy radicals; then the acrolein product velocity distribution, being intangibly altered by loss of a H atom, should be very nearly momentum matched to chlorine if the radicals of all internal energies access that product channel. Figure 5 is the TOF spectrum of acrolein with two fits. The gray solid line fit is predicted from the $P(E_T)$ in Fig. 3 derived from the entire Cl atom TOF distribution. It clearly overfits the data on the fast side, thereby demonstrating that the lowest internal energy radicals, those formed in the highest E_T photodissociation events, are formed with too little internal energy to access the H +acrolein product channel. The good fit shown by the dashed line in Fig. 5 is calculated from the $P(E_T)$ represented by the dashed line in Fig. 6 [it is superimposed on the major C–Cl bond fission $P(E_T)$'s from Fig. 3 for comparison]. In Sec. IV we describe the model that gave a good fit to the distribution
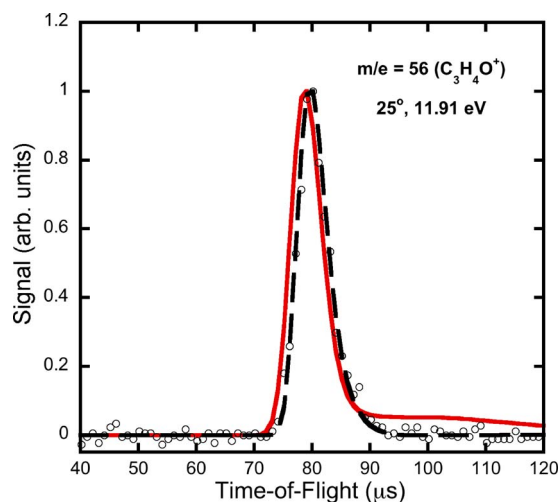
FIG. 5. (Color online) TOF spectrum for acrolein, $m/e=56$, using 11.91 eV photoionization, accumulated for 200 000 laser shots with constant background subtraction. The open circles represent the data points, and the solid line shows the poor fit to the data if one uses the entire C–Cl fission $P(E_T)$ in Fig. 3 to predict the velocity of the acrolein products (the loss of a H atom from the momentum-matched radical to the Cl atom does not appreciably alter the acrolein product velocity). The dashed line fit, calculated from the dashed line $P(E_T)$ in Fig. 6, reveals which subset of the momentum-matched radicals access the H+acrolein product channel.

of internal energies of radicals that the data show, which dissociate to form H+acrolein. It is clear that, independent of any model, the acrolein data show that the lowest internal energy radicals do not dissociate to H+acrolein; therefore the acrolein+H product channel must be accessed by a transition state that is 2–3 more kcal/mol higher in energy than the lowest dissociation channel of the radical intermediates. This result is consistent with the prediction from our CCSD(T) electronic structure results that most of the radicals dissociating to the H+acrolein product channel do so via a loose transition state 17.5 kcal/mol above the INT2 zero
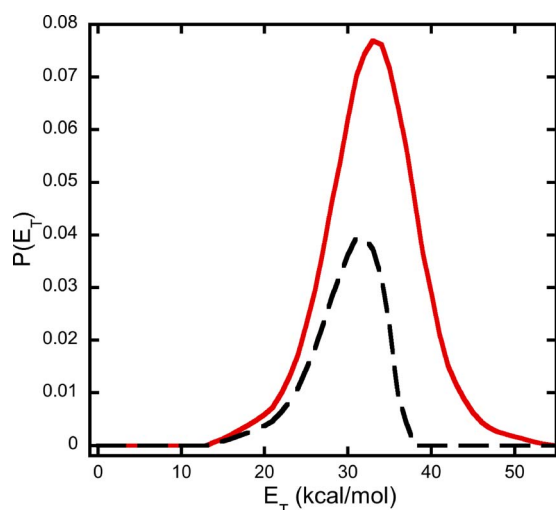

FIG. 6. (Color online) Comparison of the high KE portion of the $m/e=35$ $P(E_T)$ (solid line) and the $m/e=56$ $P(E_T)$ (dashed line). The $m/e=56$ distribution lacks the low recoil KE portion corresponding to the slow tail present in Fig. 2. The $m/e=56$ $P(E_T)$ also deviates from the $m/e=35$ $P(E_T)$ at the higher recoil translational energies, beginning at 38 kcal/mol. The relative normalization of the two $P(E_T)$'s is arbitrarily set to the statistical prediction for the product branching to the subsequent H+acrolein channel.

point level, while radicals with 2 kcal/mol lower energy can dissociate by isomerizing to INT4 and then dissociating to ethene+HCO. Thus the lowest internal energy radicals that we produce can dissociate to ethene+HCO, but not to acrolein+H, so acrolein is not formed from the fastest portion of $P(E_T)$ that produces OCH_2CHCH_2 radicals, as these radicals do not have enough vibrational energy to surmount the 17.5 kcal/mol barrier to acrolein+H.

Interestingly, the data in Fig. 5 also show that the slow broad peak present in the $m/e=35$ spectrum is absent for $m/e=56$. This absence indicates that the radical cofragments formed in conjunction with the slow Cl atoms do not significantly access the acrolein+H product channel even though they have higher internal energies than the radicals formed in the main C–Cl fission channel. This is also evident in comparing the dashed line portion of the $P(E_T)$ in Fig. 6, which fits the measured acrolein velocity distribution, with the overall C–Cl bond fission KE distribution in Fig. 3. The low KE portion of the $P(E_T)$ in Fig. 3, shown in dot-dashed line, does not result in radicals which dissociate to H+acrolein. Thus the radicals produced in this minor channel, with the low kinetic energies fitted by the small broad portion of the C–Cl bond fission $P(E_T)$ peaking near 1 kcal/mol in Fig. 3, access quite distinct dynamics from the bulk of ground state radicals produced in the major C–Cl bond fission channel. We considered the possibility that this minor channel corresponds to the formation of Cl and electronically excited C_3H_5O radicals, but no low-lying excited state of the radical emerged as a clear candidate. The unique dynamics that resulted in these very high internal energy radicals not accessing the H+acrolein product channel is still under investigation.[37]

In prior work on radical dissociation via H-atom loss, we were able to use the threshold C–Cl bond fission recoil KE at which we lost radicals to dissociation to deduce, via energy conservation, the corresponding internal energy in the radical at threshold and, thus, the barrier for H loss from the radical. However in the case of the c-OCH_2CHCH_2 radicals produced from the photodissociation of epichlorohydrin, when significant energy is partitioned to recoil KE, the large impact parameter also results in substantial energy being partitioned into rotation of the radical. If one uses a simple impulsive model assuming that the recoil KE is imparted impulsively at the equilibrium geometry of epichlorohydrin, one predicts that to conserve angular momentum the radicals must be imparted with 22 kcal/mol of rotational energy when 40 kcal/mol is partitioned to recoil KE between the radical and the Cl atom. The resulting radicals would then have large translational and rotational energies, leaving them with small amounts of vibrational energy. Hence, we did attempt to detect stable radicals even though their calculated total internal energy was above the lowest dissociation barrier. Unlike our prior work on allyl iodide photodissociation, in which we did detect allyl radicals that did not dissociate by virtue of a large portion of their internal energy being in rotation instead of in vibrational energy, we did not detect stable OCH_2CHCH_2 radicals. We conclude that the C–Cl bond fission from electronically excited epichlorohydrin accesses geometries outside the Franck–Condon region with a

smaller impact parameter before undergoing an impulsive dissociation and thus partitions a smaller fraction of the available energy to rotation. In Sec. IV we use a model with variable partitioning to rotational energy to analyze the subsequent dissociation dynamics of the OCH_2CHCH_2 radicals.

D. Identifying the C-C fission product channels from the OCH_2CHCH_2 radical intermediate

We now turn to the other product channels of the O +allyl bimolecular reaction that can potentially be accessed from the radical intermediate studied in this work; the four C–C bond fission channels are shown in Fig. 1. We can assign which of these product channels contribute significantly to the product branching from this radical intermediate by careful examination of the signal detected in our experiments at $m/e=30$, 29, 28, and 27. Figure 7 displays the TOF spectrum for each of the above masses obtained with 12.1 eV photoionization. All of them exhibit a bimodal structure with the $m/e=29$ data displaying the two peaks most clearly, which suggests that the product channels represented by the spectra are produced via two dynamical pathways. The two components in these spectra are products from both the high KE fragments formed in the dominant C–Cl bond fission channel and the low KE radicals formed in the minor component of the primary photofission $P(E_T)$ partitioning from 0 to 12 kcal/mol in product translation. The $m/e=56$ data showed that the low KE radicals do not dissociate to H +acrolein, so their branching to the C–C fission product channels is correspondingly larger.

Let us consider the C–C bond fission products from the ground state radicals produced in the dominant high recoil KE channel. Because these radicals are formed from the C–Cl bond fission events with higher recoil KEs (from 12 to 50 kcal/mol), the products from these ground state radicals would have faster velocities even though the loose transition states for the C–C bond fission channels in the ground state are not expected to release substantial energy to relative KE as these radicals dissociate. The $m/e=30$ data must correspond to the photoionization of formaldehyde product at 12.1 eV, indicating that a significant component of the product branching is to formaldehyde+C_2H_3. The $m/e=27$ data have a very similar shape to the $m/e=30$ data, as expected from a momentum-matched product in the same channel with similar mass to its coproduct. A careful analysis of the $m/e=28$ and $m/e=29$ data reveals that these are primarily due to the C_2H_4+HCO product channel, not the C_2H_5+CO product channel. The reasoning is as follows. The ionization energy of CO is 14 eV so it would not contribute to the $m/e=28$ spectrum at 12.1 eV. Progressing to the other product in that channel, ethyl radicals give substantial signal at $m/e=29$, 28, and 27 (the latter two from dissociative ionization) at high photoionization energies (e.g., 13.8 eV). However, a previous work[22] in this group showed that the dissociative ionization of ethyl radicals to $m/e=28$ is negligible at 12.1 eV, which was the ionization energy used for the data in Fig. 7. Also, the $m/e=28$ spectrum cannot result from the dissociative ionization of formaldehyde or HCO at 12.1 eV, as those appearance energies are 14.1 eV (Ref. 38)
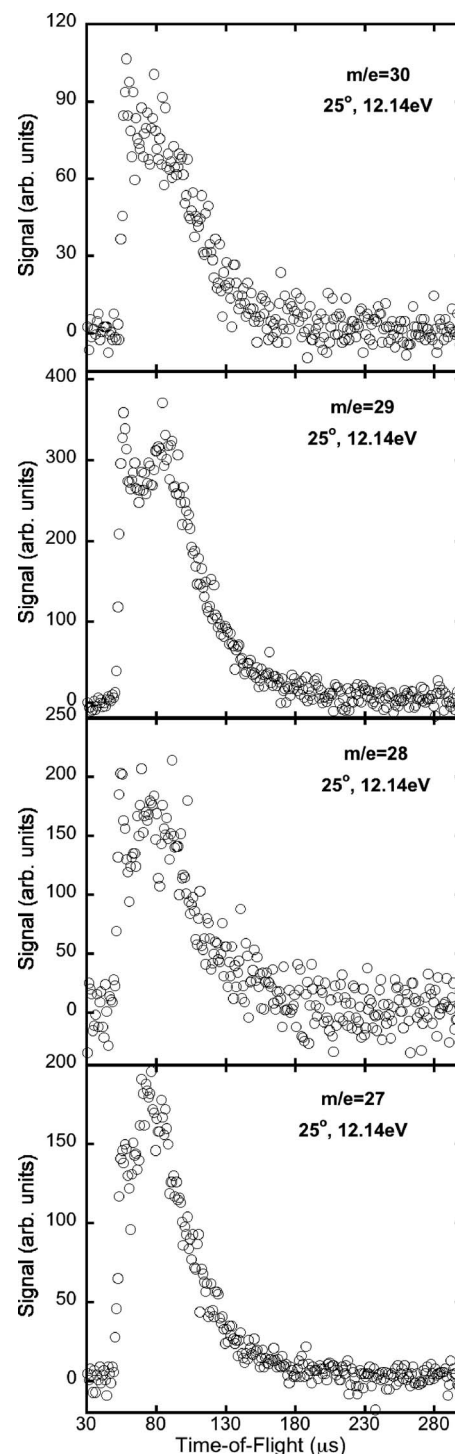

FIG. 7. TOF spectra for $m/e=30$, 29, 28, and 27 at a source angle of 25° and an ionization energy of 12.14 eV. Each set was accumulated for 200 000 shots and has the measured time-dependent background subtracted, except for $m/e=30$ spectrum that used 300 000 shots and constant background subtraction.

and 14.6 eV,[39] respectively. Dissociative ionization of acrolein at 12.1 eV could give signal at $m/e=28$, but this signal would have the same narrow velocity distribution as the signal in Fig. 5; the acrolein dissociative ionization signal, adjusting for the difference in ion flight time, would peak near 68 μs in the $m/e=28$ TOF spectrum, which lies between the two peaks in the observed signal. Thus, the majority of the signal in the $m/e=28$ data in Fig. 7 must result

from ethene, the cofragment of HCO. The momentum-matched HCO product at $m/e=29$ is expected to have a very similar TOF spectrum to the ethene spectrum at $m/e=28$ because the two products in the HCO+ethene product channel have almost the same mass, and Fig. 7 shows this is true. The $m/e=29$ data may also include contributions from dissociative ionization of formaldehyde (the appearance energy of HCO$^+$ from formaldehyde was reported near 12 eV). We conclude that C_2H_5 does not contribute significantly to the $m/e=29$ signal because our photoionization efficiency curve[37] at this mass has a much later onset than that measured by Wang *et al.*[40] for C_2H_5.

Thus, we conclude that the data in Fig. 7 mainly result from two product channels, the formaldehyde+C_2H_3 product channel, which can occur in competition with the observed acrolein+H product channels via loose transition states from INT1, and the ethene+HCO product channel, which is expected to be the dominant channel from the INT1 radicals that are able to isomerize to INT4. We do not expect significant branching to the most exothermic channel, the CO+ethyl product channel. If the barrier for isomerization of INT4 to INT5 is comparable to or higher than the barrier to dissociate directly to ethene+HCO, as predicted from the CCSD(T) calculations, one would not expect substantial branching to the CO+ethyl product channel as the tighter transition state results in smaller rate constants. We also observed a very small but non-negligible signal at ketene after integrating for 100 000 shots; this will be discussed in a later publication.[37]

E. Branching fraction to the H+acrolein product channel

The data presented herein also allow us to determine the branching fraction to the H+acrolein product channel resulting from the well-characterized internal energy distribution of the O+allyl radical intermediate under study. We can then compare this to statistical predictions for the branching fraction determined from the calculated transition states for the competing product channels. To experimentally determine the product branching fraction, we must use the results of several prior studies, as the determination requires estimating the relative photoionization cross sections of Cl atoms at 13.8 eV and of acrolein near 12 eV.

We begin by analyzing the integrated signals at $m/e=35$ from Cl atoms and $m/e=56$ from acrolein. As each neutral Cl atom produced photolytically has a radical cofragment, the branching fraction for the radical cofragments to form H+acrolein products can be determined from the ratio of acrolein product to Cl atoms. Using TOF spectra at Cl$^+$ and the acrolein cation CH$_2$CHCHO$^+$ taken consecutively and detected at 13.8 and 11.9 eV, respectively, we integrate the signal in each spectrum, normalizing each to 1000 laser shots. Then we divide each integrated signal by a correction factor that accounts for the expected signal due to the three-dimensional scattering kinematics in the photodissociation, the differing transit times through the ionization region due to the neutral fragment velocities, and the appropriate Jacobian factor. We also correct for the fraction, 0.7578, of Cl

atoms that are ^{35}Cl, as we detect the acrolein products from the radicals that are momentum matched to both isotopes of Cl but only detect ^{35}Cl. Finally, we must correct the integrated signal at each ion by the partial photoionization cross section of Cl to form Cl$^+$, σ_{Cl/Cl^+}, and CH$_2$CHCHO to form parent ion CH$_2$CHCHO$^+$, $\sigma_{C_3H_4O/C_3H_4O^+}$. Integrating the Cl$^+$ signal from channel 50 to 69 (with subtraction of the tiny overlapping signal from the minor C–Cl fission channel) and the $m/e=56$ signal from channel 70 to 95 and using the solid and dashed line $P(E_T)$'s in Fig. 6 to make the appropriate corrections for differing neutral fragment kinematics for Cl atoms and acrolein, we obtain

$$f_{H+acrolein} = \left(\frac{\text{integrated counts at } C_3H_4O^+}{\text{integrated counts at } ^{35}Cl^+}\right)\left(\frac{75.78}{100}\right)$$

$$\times \left(\frac{\text{expected Cl signal}}{\text{expected } C_3H_4O \text{ signal}}\right)\frac{\sigma_{Cl/Cl^+}}{\sigma_{C_3H_4O/C_3H_4O^+}}$$

$$= \left(\frac{5.364}{12.70}\right)\left(\frac{75.78}{100}\right)\left(\frac{0.1019}{0.2434}\right)\left(\frac{23.7}{17.8}\right) = 0.18.$$

$$(3)$$

The partial photoionization cross sections in the end of the equation above were determined as follows. Acrolein can dissociatively ionize at 12 eV. We only used the integrated signal from acrolein at $m/e=56$ (to avoid contamination by other products), so we must determine the partial photoionization cross section of CH$_2$CHCHO to CH$_2$CHCHO$^+$, $\sigma_{C_3H_4O/C_3H_4O^+}$, the product of the total photoionization cross section and the fraction of ionized species that appear at the parent ion. We did this by comparing the signal at $m/e=56$ from an acrolein beam and $m/e=28$ signal from an ethene beam detected with VUV photoionization. Photoionizing two neat molecular beams of acrolein and ethene, both with a nozzle temperature of 50 °C and a stagnation pressure of 240 torr at 12.1 eV, gave the ion relative signals determined from the average of six trials as CH$_2$CHCHO$^+$/C$_2$H$_4^+$ $=2.15\pm0.16$ (95% confidence interval). Then multiplying by 8.29 Mb, the literature photoionization cross section[41,42] of ethene at the nearest tabulated photoionization energy gives $\sigma_{C_3H_4O/C_3H_4O^+}=17.8$ Mb. (We use the most recent determination of the ethene photoionization cross section, although Grimm *et al.*[43] reported a much lower value of 4.7 Mb at 12 eV.) The value used for the photoionization cross section of Cl of 23.7 Mb at 13.8 eV is an average over the bandwidth of the photoionization source at the NSRRC; its determination is described in detail in Ref. 22, putting this cross section on the same scale as a recent determination[44] of the photoionization cross sections of vinyl and propargyl radicals. Thus this cross section will also be useful in determining the branching fraction to the H$_2$CO+C$_2$H$_3$ product channel presently underway.

F. Velocity map imaging of the Cl($^2P_{3/2}$) and Cl($^2P_{1/2}$) components

Returning to the chlorine spectra, the ion images of the Cl($^2P_{3/2}$) and Cl($^2P_{1/2}$) photofragments are shown in Figs. 8(a) and 8(b), respectively, with the 235 nm laser

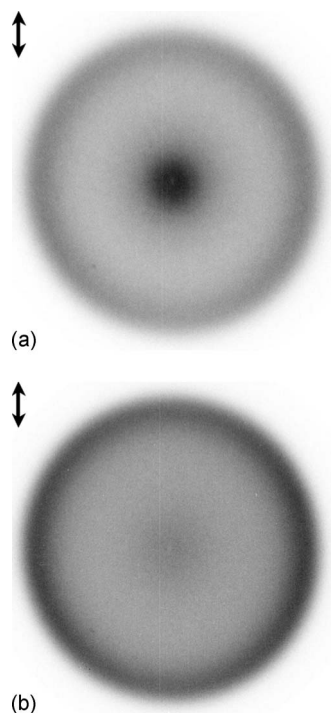FIG. 8. The upper frame shows the raw image of $Cl(^2P_{3/2})$ obtained by photodissociating at 193.3 nm and probing with 235.34 nm via the $4p\,^2D_{3/2} \leftarrow 3p\,^2P_{3/2}$ transition. The lower frame shows the raw image of $Cl(^2P_{1/2})$ obtained by photodissociating at 193.3 nm and probing with 235.20 nm via the $4p\,^2P_{1/2} \leftarrow 3p\,^2P_{1/2}$ transition. The laser polarization is in the vertical direction as marked by the double-headed arrow, and each raw image is 861×861 pixels.

polarization direction along the vertical axis. Each image displays a dominant high KE release component; the minor low recoil KE C–Cl bond fission channel produces radicals in conjunction with $Cl(^2P_{3/2})$. The speed distributions of the $Cl(^2P_{1/2,3/2})$ fragments are extracted by integrating the three-dimensional speed distributions over all solid angles at each speed, and the total center-of-mass translational energy distributions, $P(E_T)$'s, are derived from the $Cl(^2P_{1/2,3/2})$ atom speed distributions using conservation of momentum and correcting for the appropriate Jacobian. The results are presented in Fig. 9, where the peak value of translational energy release in the C–Cl fission channel that produces $Cl(^2P_{3/2})$ atoms is 32.0 kcal/mol, and that producing $Cl(^2P_{1/2})$ is 34.0 kcal/mol.

Similar to the consistency check between the tunable VUV and electron impact ionization data, the $P(E_T)$'s for the velocity map imaging and the tunable VUV are compared in Fig. 10. The degree of similarity between the two translational energy distributions is remarkable. Gross features such as the main peak and its width are nearly identical. The only differences arise in the smaller KE portion of the distributions where the velocity map imaging distribution is slightly lower around 16 kcal/mol.

State-selective detection methods of $Cl(^2P_{3/2})$ and $Cl(^2P_{1/2})$, such as REMPI, provide a means for measuring the relative populations of the fine-structure states of the chlorine photofragments. Detection of $Cl(^2P_{1/2})$ via the $4p\,^2P_{1/2} \leftarrow 3p\,^2P_{1/2}$ scheme is more efficient than the detection of $Cl(^2P_{3/2})$ using the $4p\,^2D_{3/2} \leftarrow 3p\,^2P_{3/2}$ transition, so
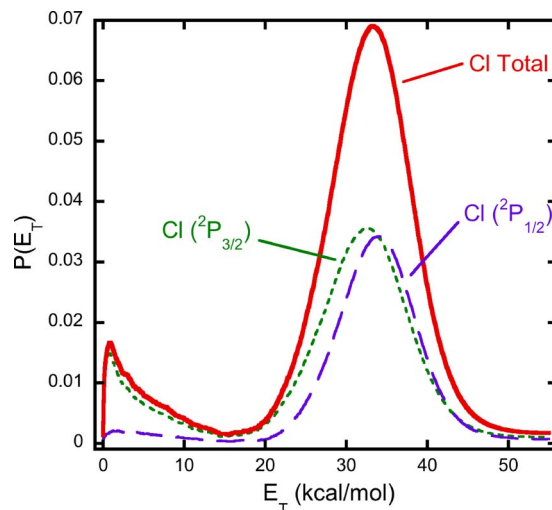

FIG. 9. (Color online) Total center-of-mass translational energy distributions for the ground (dotted line) and excited (dashed line) states of chlorine, $m/e=35$. The overall fit, after accounting for the proper line strength factor (Ref. 45) is given by the solid line.

the fraction of ground state chlorine must be increased to compensate for the difference. Equation (4) illustrates the above calculation,

$$\frac{N(Cl^*)}{N(Cl)} = \frac{S(Cl^*)}{S(Cl)} \frac{LS(Cl)}{LS(Cl^*)}. \tag{4}$$

The ratio $N(Cl^*)/N(Cl)$ is the relative spin-orbit branching in which we are interested. $S(Cl^*)/S(Cl)$ is the measured branching ratio between the states without correction for differing REMPI detection efficiencies. It is obtained by integrating the chlorine ion signal intensity over the entire velocity range. Lastly, $LS(Cl)/LS(Cl^*) \equiv f$ is the line strength factor, where $f=0.85$, as determined by Liyanage et al.[45] Utilizing the above equation, the measured ion signal ratio, $Cl^*/Cl=0.89 \pm 0.15$, and the line strength factor, the branch-
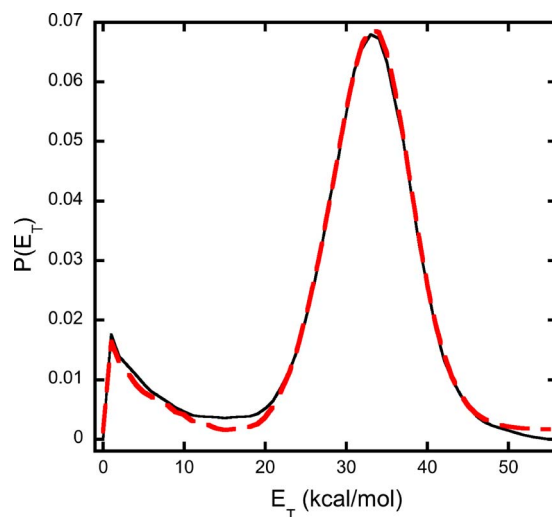

FIG. 10. (Color online) Comparison of the recoil translational energy distributions for $m/e=35$ using tunable VUV detection or velocity map imaging with REMPI ionization. The solid line corresponds to the distribution from the crossed laser-molecular beam apparatus having tunable VUV ionization, and the dashed line corresponds to the velocity map imaging distribution.

ing ratio for $Cl(^2P_{1/2})/Cl(^2P_{3/2})$ is 0.76 ± 0.17, and the resulting quantum yields are $\Phi[Cl(^2P_{1/2})]=0.43 \pm 0.02$ and $\Phi[Cl(^2P_{3/2})]=0.57 \pm 0.02$. Note that this ratio would be much different for the slow tail as shown in Fig. 9 where ground spin-orbit state chlorine dominates.

IV. DISCUSSION

Many elementary bimolecular reactions, including the reaction of O atoms with allyl radicals studied here, can proceed by two qualitatively distinct mechanisms: addition/elimination and direct abstraction. An addition mechanism forms vibrationally excited radical intermediates whose subsequent isomerization and dissociation dynamics determine the final product branching for the bimolecular reaction. To probe a key portion of these dynamics, our experimental methodology generates a particular isomeric form of an unstable radical intermediate along a bimolecular reaction coordinate under collisionless conditions and investigates the branching between the ensuing product channels of the energized radical as a function of its internal energy. The data probe the barriers encountered by the radical intermediates as each proceeds toward one of the product channels of the bimolecular reaction, providing key benchmarks for emerging electronic structure calculations on reactions proceeding through radical intermediates. The methodology can probe the dynamics resulting from each of several possible radical intermediates, thereby offering key observables for comparison with statistical or classical and quantum reactive scattering dynamics predictions on the potential energy surface(s) of the bimolecular reaction.

While the H+acrolein channel was understood to be an important product channel of the O+allyl reaction, the work presented here definitively assigned the other major product channels accessed by addition of the O atom to an end carbon atom of the allyl radical. Our data showed that the $H_2CO+C_2H_3$ and the C_2H_4+HCO product channels contribute substantially to the product branching along with H+acrolein, but the most exothermic product channel, C_2H_5+CO, probably does not. These results are in accord with the predicted transition states en route to products calculated at the CCSD(T) level of theory shown in Fig. 1. The radical formed by addition of the O atom to an end C atom, INT1 in Fig. 1, can dissociate directly to the formaldehyde+C_2H_3 product channel or the acrolein+H product channel via two loose transition states, or it can isomerize to the radical labeled INT4 in Fig. 1. The fraction of radicals that isomerize to INT4, CH_2CH_2CHO, predominantly dissociates directly to C_2H_4+HCO, the third major product channel observed in our work, via a loose transition state of low energy. The fact that we observe no significant branching to the most exothermic channel, the ethyl+CO product channel, is easily understood by considering the calculated transition states from the INT4, CH_2CH_2CHO, radical intermediate. In order to result in ethyl+CO, this radical must first undergo a 1,3-H-atom shift, but the barrier for that isomerization is calculated to be much higher than the barrier to dissociate directly to ethene+HCO. The former has a tight transition state, while the latter has a loose one, so even under the higher energy

conditions of dynamics beginning in the O+allyl reactant asymptote, one would not expect significant branching to the ethyl+CO product channel.

A powerful feature of our experimental method is that the data reveal which internal energy radicals dissociated to the H+acrolein product channel. This is accomplished by comparing the velocity distribution of the acrolein product to the velocity distribution of the nascent radicals. (The latter is determined as the radicals are momentum matched to the detected halogen cofragment, thereby yielding the internal energy distribution of all the radicals, whether they dissociate or not.) The data detailed in Sec. IV C showed that the lowest internal energy radicals did not dissociate to H+acrolein; this is consistent with the calculated CCSD(T) transition state for INT1→acrolein+H being higher than the isomerization barrier to INT4, which goes on to dissociate to C_2H_4+HCO. The shape of the velocity distribution of the acrolein products can also reveal the internal energy dependence of the branching fraction to the acrolein+H product channel as described below.

A more quantitative analysis of the product branching to the acrolein+H channel requires careful consideration of the nature of the internal energy distribution of the initial radical adduct, INT1, formed in these experiments. While we determined this internal energy distribution directly from our experimental data via energy conservation (the determination relies on an accurate C–Cl bond energy of the precursor), one must consider the fraction of internal energy partitioned to rotational energy versus vibrational energy of the radical. After accounting for this internal energy partitioning, one can then compare the measured product branching with a statistical prediction of the product branching averaged over the internal energy distribution of the nascent radicals. To begin such an analysis, we first recognize that if the dynamics of the excited C–Cl bond fission channel in the photolytic precursor of the radical is well represented by an impulsive dissociation from the ground state equilibrium geometry of the precursor, one would expect a large fraction of the available energy to be partitioned to radical rotation (as the impact parameter is large because the chlorine is bonded to a terminal C atom). Indeed, a simple impulsive model from this geometry predicts that if 40 kcal/mol is partitioned to relative KE, 22 kcal/mol must be partitioned to rotational energy to conserve angular momentum, leaving the nascent radicals with too little energy to dissociate. Clearly the C–Cl bond fission in epichlorohydrin does not occur impulsively from the equilibrium geometry of ground state epichorohydrin; this would only be expected if the excited state were purely repulsive in character. The excited state of epichlorohydrin accessed at 193.3 nm is not a repulsive $n \to \sigma^*$ excited state in the Franck–Condon region; it is an excited state that is locally bonding in the C–Cl bond, so the impulsive dynamics is generated in a region of the excited state outside the Franck–Condon region. One can thus expect the partitioning to rotational energy to be quite different. Nevertheless, when the dissociative trajectories do access a portion of the excited state that is repulsive and generate substantial relative velocity between the Cl and radical cofragments, in a classical model one must conserve angular
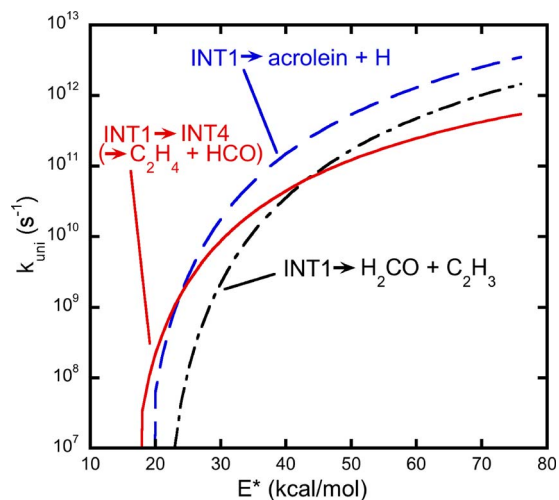
FIG. 11. (Color online) Statistical rate constants predicted for the unimolecular dissociation of the INT 1 radical intermediate for the three dominant product channels observed in this work. The barriers used are those shown in Fig. 1, adjusted for the 1.81 kcal/mol energy difference between INT1 and INT2.

momentum, so some energy is partitioned to radical rotation. If one retains an impulsive model using whatever geometry the excited state dynamics encounters repulsive forces, one predicts that the energy partitioned to product rotation must increase linearly with the translational energy release in order to conserve angular momentum. We take this feature into account explicitly in the analysis below by requiring the energy partitioned to rotational energy of the radical be a constant fraction of the measured E_T, and at each E_T we subtract this rotational energy from the internal energy of the radical calculated by Eq. (2). In this way we account for the energy partitioned to rotation of the radical during its photolytic generation.

One can compare the branching fraction to the acrolein +H product channel measured in these experiments to the predictions from simple statistical theories as follows. We first use three of the transition states calculated at the RCCSD(T)/aug-cc-pVQZ‖UCCSD/aug-cc-pVDZ level of theory to calculate[46] the unimolecular rate constants for the three dominant product channels accessed by this radical intermediate as a function of internal energy E^* in the INT1 radical. E^* in the calculation is the E_{int} described in Eq. (2) plus the 1.81 kcal/mol energy difference between INT1 and INT2, less the energy partitioned impulsively to rotation in the photolytic generation of the radical. We take the last as $0.4E_T$, as that proportionality constant resulted in a good fit of the leading edge of our detected acrolein spectrum in Fig. 5. (This rotational energy partitioning is less than that if the impulsive force was generated in the vertical geometry on the excited state surface, but is still substantial.) The predicted statistical rate constants are shown in Fig. 11. The product branching prediction is sensitive to only the relative values, not the absolute values, of these rate constants (as in the RRKM expression the density of states of the molecule at energy E^* is the divisor for all the calculated rate constants), so the horrors of assuming a harmonic density of states is mitigated. The RRKM analysis, assuming that the impulsive

rotational partitioning is $0.4E_T$, predicts that the product branching to the acrolein+H product channel (averaged over the internal energy distribution of radicals generated in the high KE C–Cl fission channel) would be 0.38. This is a factor of 2 larger than the experimentally determined branching fraction of 0.18 to the acrolein+H product channel. This RRKM-based analysis neglected any contribution from tunneling through the INT1 to INT4 isomerization barrier, but such tunneling would give a larger branching to the C_2H_4 +HCO product channel at the expense of stable radicals, not at the expense of branching to the acrolein+H product channel. The experimental branching fraction does not rely on any assumption of rotational energy partitioning to the radical, but the results of the RRKM analysis do. If that estimate and the ethene photoionization cross section on which we base the analysis of our observed acrolein signal are correct, the branching ratio comparison suggests that the INT1 →INT4 isomerization barrier calculated here is too high (a lower isomerization barrier would allow the ethene+HCO channel to compete more effectively with the acrolein+H channel, thereby bringing the theoretical prediction closer to the experimental result).

It is interesting to note that the velocity map imaging $m/e=35$ $P(E_T)$ in Fig. 9 shows a distinct difference between the fraction of ground state chlorine atoms formed in coincidence with the low and high recoil KE radicals. Namely, high recoil KE radicals form in conjunction with both ground and spin-orbit excited chlorine atoms, while the low recoil KE radicals are almost exclusively generated with ground spin-orbit state chlorine atoms. In several earlier studies, we were able to definitively assign the low recoil KE channel to one that produces an electronically excited radical+Cl, and noted that Cl in this channel was predominantly in the ground spin-orbit state.[47–49] Thus, we did consider the possibility that the low recoil KE C–Cl bond fission channel in this study gives electronically excited radicals. However, two-state MCSCF calculations using several active spaces did not reveal any excited states that would be energetically accessible for INT2. The lack of an accessible excited state at the ground state geometry of INT2 suggests that ring opening could occur simultaneously with photodissociation because the first excited state falls from >100 kcal/mol at INT2 to 3 kcal/mol at INT1. A definitive assignment thus cannot be made; more calculations are required in order to study higher lying excited states and the epichlorohydrin precursor.

Similar experiments utilizing Raman-shifted photodissociation light at 210 nm could simplify some of the results by reducing or removing the contribution of high internal energy radicals that are momentum matched to the slow chlorine atoms in Fig. 1. The longer wavelength might also allow the detection of stable C_3H_5O radicals, thereby facilitating an accurate experimental estimate for the product channel having the lowest barrier height.

ACKNOWLEDGMENTS

[1] C. S. McEnally, L. D. Pfefferle, B. Atakan, and K. Kohse-Hoinghaus, Prog. Energy Combust. Sci. **32**, 247 (2006).

[2] J. W. Bozzelli and A. M. Dean, J. Phys. Chem. **97**, 4427 (1993).

[3] J. Lee and J. W. Bozzelli, Proc. Combust. Inst. **30**, 1015 (2005).

[4] R. P. Ruiz, K. D. Bayes, M. T. Macpherson, and M. J. Pilling, J. Phys. Chem. **85**, 1622 (1981).

[5] N. M. Marinov, M. J. Castaldi, C. F. Melius, and W. Tsang, Combust. Sci. Technol. **128**, 295 (1997).

[6] N. M. Marinov, W. J. Pitz, C. K. Westbrook, A. M. Vincitore, M. J. Castaldi, S. M. Senkan, and C. F. Melius, Combust. Flame **114**, 192 (1998).

[7] C. S. McEnally and L. D. Pfefferle, Combust. Flame **143**, 246 (2005).

[8] I. R. Slagle, J. R. Bernhardt, D. Gutman, M. A. Hanning-Lee, and M. J. Pilling, J. Phys. Chem. **94**, 3652 (1990).

[9] H.-C. Kwon, J.-H. Park, H. Lee, H.-K. Kim, Y.-S. Choi, and J.-H. Choi, J. Chem. Phys. **116**, 2675 (2002).

[10] J.-H. Park, H. Lee, H.-C. Kwon, H.-K. Kim, Y.-S. Choi, and J.-H. Choi, J. Chem. Phys. **117**, 2017 (2002).

[11] S.-K. Park, L.-K. Kwon, H. Lee, and J.-H. Choi, J. Chem. Phys. **120**, 7976 (2004).

[12] J.-H. Choi, Int. Rev. Phys. Chem. **25**, 613 (2006).

[13] J.-H. Park, H. Lee, and J.-H. Choi, J. Chem. Phys. **119**, 8966 (2003).

[14] N. Balucani and P. Casavecchia, AIP Conf. Proc. **CP855**, 17 (2006).

[15] F. Leonori, N. Balucani, G. Capozza, E. Segoloni, D. Stranges, and P. Casavecchia, Phys. Chem. Chem. Phys. **9**, 1307 (2007).

[16] L. J. Butler and D. M. Neumark, J. Phys. Chem. **100**, 12801 (1996).

[17] C. C. Wang, Y. T. Lee, J. J. Lin, J. Shu, Y. Y. Lee, and X. J. Yang, J. Chem. Phys. **117**, 153 (2002).

[18] S.-H. Lee, Y.-Y. Lee, Y. T. Lee, and X. Yang, J. Chem. Phys. **119**, 827 (2003).

[19] J. J. Lin, Y. Chen, Y. Y. Lee, Y. T. Lee, and X. Yang, Chem. Phys. Lett. **361**, 374 (2002).

[20] X. Yang, J. Lin, Y. T. Lee, D. A. Blank, A. G. Suits, and A. M. Wodtke, Rev. Sci. Instrum. **68**, 3317 (1997).

[21] Y. T. Lee, J. D. McDonald, P. R. LeBreton, and D. R. Herschbach, Rev. Sci. Instrum. **40**, 1402 (1969).

[22] B. L. FitzPatrick, M. Maienschein-Cline, L. J. Butler, S.-H. Lee, and J. J. Lin, J. Phys. Chem. A **111**, 12417 (2007).

[23] N. R. Daly, Rev. Sci. Instrum. **31**, 264 (1960).

[24] A. J. R. Heck and D. W. Chandler, Annu. Rev. Phys. Chem. **46**, 335 (1995).

[25] A. T. J. B. Eppink and D. H. Parker, Rev. Sci. Instrum. **68**, 3477 (1997).

[26] Y. Sato, Y. Matsumi, M. Kawasaki, K. Tsukiyama, and R. Bersohn, J. Phys. Chem. **99**, 16307 (1995).

[27] K. C. Lau, Y. Liu, and L. J. Butler, J. Chem. Phys. **123**, 054322 (2005).

[28] Y. Liu and L. J. Butler, J. Chem. Phys. **121**, 11016 (2004).

[29] Y. Liu, K. C. Lau, and L. J. Butler, J. Phys. Chem. A **110**, 5379 (2006).

[30] V. Dribinski, A. Ossadtchi, V. A. Mandelshtam, and H. Reisler, Rev. Sci. Instrum. **73**, 2634 (2002).

[31] A. G. Baboul, L. A. Curtiss, P. C. Redfern, and K. Raghavachari, J. Chem. Phys. **110**, 7650 (1999).

[32] L. A. Curtiss, P. C. Redfern, V. Rassolov, G. Kedziora, and J. A. Pople, J. Chem. Phys. **114**, 9287 (2001).

[33] M. J. Frisch, G. W. Trucks, H. B. Schlegel *et al.*, GAUSSIAN03, Revision C.02, Gaussian, Inc., Pittsburgh, PA, 2003.

[34] MOLPRO, version 2006.1, a package of *ab initio* programs, designed by H.-J. Werner, P. J. Knowles, R. Lindh, F. R. Manby, M. Schütz *et al.* (see http://www.molpro.net).

[35] P. J. Knowles, C. Hampel, and H.-J. Werner, J. Chem. Phys. **99**, 5219 (1993); **112**, 3106E (2000).

[36] See EPAPS Document No. E-JCPSA6-129-603832 for structures, energies (without zero point correction), unscaled vibrational frequencies, and moments of inertia of the intermediates and transition states calculated for the O+allyl reaction at the RCCSD(T)/aug-cc-pVQZ∥UCCSD/aug-cc-pVDZ level of theory. For more information on EPAPS, see http://www.aip.org/pubservs/epaps.html.

[37] B. L. FitzPatrick, L. J. Butler, S.-H. Lee, and J. J. Lin (in preparation).

[38] P. M. Guyon, W. A. Chupka, and J. Berkowitz, J. Chem. Phys. **65**, 1419 (1976).

[39] B. Ruscic, personal communication, September 2007. These are unpublished interim results from the Active Thermochemical Tables (ATcT) ver. 1.36 and the Core (Argonne) Thermochemical Network, ver. 1.064.

[40] J. Wang, L. Wei, B. Yang *et al.*, Chem. Res. Chin. Univ. **22**, 375 (2006).

[41] J. C. Person and P. P. Nicole, J. Chem. Phys. **49**, 5421 (1968).

[42] T. A. Cool, J. Wang, K. Nakajima, C. A. Taatjes, and A. Mcllroy, Int. J. Mass. Spectrom. **247**, 18 (2005).

[43] F. A. Grimm, T. A. Whitley, P. R. Keller, and J. W. Taylor, Chem. Phys. **154**, 303 (1991).

[44] J. C. Robinson, N. E. Sveum, and D. I. M. Neumark, J. Chem. Phys. **119**, 5311 (2003).

[45] R. Liyanage, T.-A. Yang, S. Hashimoto, R. J. Gordon, and R. W. Field, J. Chem. Phys. **103**, 6811 (1995).

[46] The RRKM code is obtained from W. L. Hase and D. L. Bunker, *Quantum Chemistry Program Exchange 234* (1974). To calculate the sums and densities of states, we used the Whitten Rabinovitch semiclassical technique implemented in that software.

[47] M. J. Bell, K.-C. Lau, M. J. Krisch, D. I. G. Bennett, L. J. Butler, and F. Weinhold, J. Phys. Chem. A **111**, 1762 (2007).

[48] L. R. McCunn, M. J. Krisch, K. Takematsu, L. J. Butler, and J. Shu, J. Phys. Chem. A **108**, 7889 (2004).

[49] D. E. Szpunar, J. L. Miller, L. J. Butler, and F. Qi, J. Chem. Phys. **120**, 4223 (2004).